

Non-Fermi liquids from holography

Hong Liu, John McGreevy, and David Vegh

Center for Theoretical Physics, Massachusetts Institute of Technology, Cambridge, Massachusetts 02139, USA

(Received 7 January 2011; published 28 March 2011)

We report on a potentially new class of non-Fermi liquids in $(2 + 1)$ -dimensions. They are identified via the response functions of composite fermionic operators in a class of strongly interacting quantum field theories at finite density, computed using the AdS/CFT correspondence. We find strong evidence of Fermi surfaces: gapless fermionic excitations at discrete shells in momentum space. The spectral weight exhibits novel phenomena, including particle-hole asymmetry, discrete scale invariance, and scaling behavior consistent with that of a critical Fermi surface postulated by Senthil.

DOI: [10.1103/PhysRevD.83.065029](https://doi.org/10.1103/PhysRevD.83.065029)

PACS numbers: 11.25.Tq, 04.50.Gh, 71.10.Hf

I. INTRODUCTION

The normal state of the high- T_C superconducting cuprates, and metals close to a quantum critical point, are examples of non-Fermi liquids, which have sharp Fermi surfaces but whose low-energy properties differ significantly from those predicted from Landau's Fermi liquid theory [1–3]. While Landau Fermi liquids are controlled by a free Fermi gas fixed point with (almost) no relevant perturbations [4–7], a proper theoretical framework characterizing non-Fermi liquid metals, which likely involves strong couplings, is lacking. In this paper we search for new universality classes of non-Fermi liquids using the AdS/CFT correspondence [8–10].

According to the correspondence, any (quantum) gravity theory in a $(d + 1)$ -dimensional asymptotically anti-de Sitter (AdS_{d+1}) spacetime is dual to a d -dimensional quantum field theory “living at its boundary.” Through the AdS/CFT dictionary, a gravity theory can (in principle) be used to obtain all physical observables of its boundary dual, like the physical spectrum and correlation functions. Compared to conventional approaches, the gravity approach offers some remarkable features which make it a valuable tool for discovering new strongly coupled phenomena:

- (1) At small curvature and low energies known gravity theories reduce to a universal sector: classical Einstein gravity plus matter fields. Through the duality, this limit typically translates into the strong-coupling and large- N limit of the boundary theory, where N characterizes the number of species. Thus by working with Einstein gravity (plus various matter fields) one can extract certain universal properties of a large number of *strongly coupled* quantum field theories.¹
- (2) Highly dynamical, strong-coupling phenomena in the dual field theories can often be understood on the gravity side using simple geometric pictures.

¹The field theory origin of such universality is still rather mysterious.

Familiar examples include confinement and chiral symmetry breaking in a non-Abelian gauge theory.

- (3) Putting the boundary theory at finite temperature and finite density corresponds to putting a black hole in the bulk geometry. Questions about complicated many-body phenomena at strong coupling can be answered by solving linear wave equations in this black hole background.

Consider a quantum field theory which contains fermions charged under a global $U(1)$ symmetry.² When a finite $U(1)$ charge density is introduced into such a theory, it is natural to ask whether the system possesses a Fermi surface and if yes, what are the low-energy excitations. One approach to these questions is to study spectral functions of a fermionic composite operator.³ The presence of a Fermi surface may be revealed by the appearance of gapless excitations of the operator at discrete shells in momentum space.

This will be the approach taken here. We obtain the spectral functions for fermionic operators using the classical Einstein gravity. We will work in $(2 + 1)$ dimensions and leave other-dimensional theories for future study. While the string theory landscape in principle provides a large number of AdS/CFT dual pairs, only a few explicit examples are understood in detail; in $(2 + 1)$ -dimensions, these include the $\mathcal{N} = 8$ M2-theory and recently discovered ABJM theories [11–13]. As emphasized earlier, however, by working with the classical Einstein gravity we are extracting universal properties of a large number of boundary field theories, even if their explicit Hamiltonians are not known. The spectral functions we find give strong indications of the presence of Fermi surfaces of some non-Fermi liquid. We find poles representing “marginal”

²The theory may also contain charged scalars, and both scalars and fermions may couple additionally to some non-Abelian gauge bosons.

³The spectral function of an operator is a measure of the density of states which couple to the operator. It is proportional to the imaginary part of the retarded function G_R of the operator in momentum space.

quasiparticles at discrete shells in momentum space, with scaling behavior different from that of a Landau quasiparticle. We also observe some other novel phenomena, including particle-hole asymmetry and discrete scale invariance for a continuous range of momenta.

Our investigation was motivated in part by earlier work of Sung-Sik Lee [14], which initiated the study of spectral functions of fermionic operators using a gravity dual. Our results differ from those of [14]; we believe the difference lies in the implementation of the real-time holographic prescription [15–17].

The plan of the paper is as follows. In the next section we set up the framework for calculating the spectral functions of a fermionic operator at finite density using the gravity description. In Sec. III we discuss properties of the spectral functions, including scaling behavior near a Fermi surface. We conclude in Sec. IV with a discussion of the interpretation of the results and possible caveats.

II. SETUP OF THE CALCULATION

Consider a three-dimensional relativistic conformal field theory (CFT) with a global $U(1)$ symmetry that has a gravity dual. Such a system at finite charge density can be described by a charged black hole in four-dimensional anti-de Sitter spacetime (AdS₄) [18], with the current J_μ in the CFT mapped to a $U(1)$ gauge field A_M in AdS. A fermionic operator \mathcal{O} in the CFT with charge q and conformal dimension Δ is mapped to the gravity side to a spinor field ψ with charge q and a mass

$$mR = \Delta - \frac{3}{2} \quad (1)$$

where R is the AdS curvature radius. The spectral function of \mathcal{O} at finite charge density can then be extracted by solving the Dirac equation for ψ in the charged AdS black hole geometry. Which pairs of (q, Δ) arise depends on the specific dual CFT. However, since we are working with a universal sector common to many gravity theories, we will take the liberty of considering an arbitrary pair of (q, Δ) , scanning many possible CFTs.

A. Black hole geometry

The action for a vector field A_M coupled to AdS₄ gravity can be written as

$$S = \frac{1}{2\kappa^2} \int d^4x \sqrt{-g} \left[\mathcal{R} - \frac{6}{R^2} - \frac{R^2}{g_F^2} F_{MN} F^{MN} \right] \quad (2)$$

where g_F^2 is an effective dimensionless gauge coupling.⁴ The equations of motion following from (2) are solved by the geometry of a charged black hole [18,19]⁵

⁴It is defined so that for a typical supergravity Lagrangian it is a constant of order $\mathcal{O}(1)$.

⁵For a generic embedding of (2) into 4d $\mathcal{N} = 2$ supergravity, this solution can be lifted to an M-theory solution [20].

$$ds^2 = \frac{r^2}{R^2} (-f dt^2 + dx_i^2) + \frac{R^2 dr^2}{r^2 f} \quad (3)$$

with

$$f = 1 + \frac{Q^2}{r^4} - \frac{M}{r^3}, \quad A_0 = \mu \left(1 - \frac{r_0}{r} \right), \quad \mu \equiv \frac{g_F Q}{R^2 r_0} \quad (4)$$

where r_0 is the horizon radius determined by $f(r_0) = 0$, and μ can be identified as the chemical potential of the boundary theory. For calculational purposes it is convenient to use dimensionless quantities. Consider the rescaling

$$r \rightarrow r_0 r, \quad (t, \vec{x}) \rightarrow \frac{R^2}{r_0} (t, \vec{x}), \quad A_0 \rightarrow \frac{r_0}{R^2} A_0, \quad (5)$$

$$M \rightarrow M r_0^3, \quad Q \rightarrow Q r_0^2$$

after which the metric becomes

$$\frac{ds^2}{R^2} \equiv g_{MN} dx^M dx^N = r^2 (-f dt^2 + d\vec{x}^2) + \frac{1}{r^2} \frac{dr^2}{f}, \quad (6)$$

with now the horizon at $r = 1$ and

$$f = 1 + \frac{Q^2}{r^4} - \frac{1 + Q^2}{r^3}, \quad A_0 = \mu \left(1 - \frac{1}{r} \right), \quad (7)$$

$$\mu = g_F Q.$$

The dimensionless temperature is given by

$$T = \frac{1}{4\pi} (3 - Q^2). \quad (8)$$

The zero-temperature limit is obtained by setting $Q = \sqrt{3}$. At zero temperature, near the horizon the metric (6) becomes AdS₂ \times \mathbb{R}^2 with the curvature radius of AdS₂ given by

$$R_2 = \frac{R}{\sqrt{6}}. \quad (9)$$

B. Dirac equation

To compute the spectral functions for \mathcal{O} we need only the quadratic action of ψ in the geometry (6)–(9)

$$S_{\text{spinor}} = \int d^{d+1}x \sqrt{-g} i(\bar{\psi} \Gamma^M \mathcal{D}_M \psi - m \bar{\psi} \psi) \quad (10)$$

where

$$\bar{\psi} = \psi^\dagger \Gamma^t, \quad \mathcal{D}_M = \partial_M + \frac{1}{4} \omega_{abM} \Gamma^{ab} - iq A_M \quad (11)$$

and ω_{abM} is the spin connection.⁶ Note that the Dirac action (10) depends on q only through

$$\mu_q \equiv \mu q = g_F q Q \quad (12)$$

⁶We will use M and a, b to denote bulk spacetime and tangent space indices, respectively, and $\mu, \nu \dots$ to denote indices along the boundary directions, i.e. $M = (r, \mu)$. All indices on Gamma matrices refer to tangent space ones. For notational convenience below we will take m to be defined in units of $1/R$, i.e. $mR \rightarrow m$.

i.e. through the combination of $g_F q$. This is expected; μ is the minimal amount energy needed to add a unit charge to the system, thus for a field of charge q , the effective chemical potential is given by μ_q . Below, for notational simplicity, we will set $g_F = 1$ and treat q as a free parameter, but one should keep in mind only the product of them is the relevant quantity.

To analyze the Dirac equations following from (10), it is convenient to use the following basis

$$\Gamma^r = \begin{pmatrix} 1 & 0 \\ 0 & -1 \end{pmatrix}, \quad \Gamma^\mu = \begin{pmatrix} 0 & \gamma^\mu \\ \gamma^\mu & 0 \end{pmatrix}, \quad \psi = \begin{pmatrix} \psi_+ \\ \psi_- \end{pmatrix} \quad (13)$$

where ψ_\pm are two-component spinors and γ^μ are gamma matrices of the (2 + 1)-dimensional boundary theory. Writing

$$\psi_\pm = (-g g^{rr})^{-(1/4)} e^{-i\omega t + ik_i x^i} \phi_\pm, \quad (14)$$

the Dirac equation becomes

$$\sqrt{\frac{g_{ii}}{g_{rr}}} (\partial_r \mp m \sqrt{g_{rr}}) \phi_\pm = \mp i K_\mu \gamma^\mu \phi_\mp, \quad (15)$$

with

$$K_\mu(r) = (-u(r), k_i), \quad u = \sqrt{\frac{g_{ii}}{-g_{tt}}} \left(\omega + \mu_q \left(1 - \frac{1}{r} \right) \right). \quad (16)$$

Note that since as $r \rightarrow \infty$, $u \rightarrow \omega + \mu_q$, ω should correspond to the difference of the boundary theory frequency from μ_q , i.e. $\omega = 0$ corresponds to the Fermi energy.

To extract the retarded Green function for \mathcal{O} , we need to solve (15) with the in-falling boundary condition at the horizon [15], and to identify the source and the expectation value for \mathcal{O} from the asymptotic behavior of ψ near the boundary. Such an identification can be carried out from the prescription of [16,17], which amounts to identifying ψ_+ as the source and its canonical momentum in terms of r -slicing (which is essentially ψ_-) as the expectation value. More explicitly, ϕ_\pm have the following asymptotic behavior near $r \rightarrow \infty$,

$$\phi_+ = A r^m + B r^{-m-1}, \quad \phi_- = C r^{m-1} + D r^{-m} \quad (17)$$

with

$$C = \frac{i \gamma^\mu k_\mu}{2m-1} A, \quad B = \frac{i \gamma^\mu k_\mu}{2m+1} D, \quad k_\mu = (-(\omega + \mu_q), k_i). \quad (18)$$

Suppose the coefficients D (corresponding to expectation value) and A (corresponding to source) are related by $D = SA$, then the retarded Green function G_R is given by [17]⁷

⁷Here we assume $m \geq 0$. For $m < 0$, one simply exchanges the roles of A and D . For $m \in [0, \frac{1}{2})$, both quantization procedures are allowed. Also note that the factor γ^0 in (19) comes from $G_R \sim \langle \{ \mathcal{O}, \mathcal{O}^\dagger \} \rangle$ while in perturbing the boundary action we add $-i \int d^3x (\bar{\psi}_0 \mathcal{O} + \bar{\mathcal{O}} \psi_0)$ with $\bar{\mathcal{O}} = \mathcal{O}^\dagger \gamma^0$. As noted in [17], we must choose the sign of the overall gravity action to be consistent with unitarity.

$$G_R = -i S \gamma^0. \quad (19)$$

Eqs. (15) can be further simplified by choosing the basis $\gamma^0 = i\sigma_2$, $\gamma^1 = \sigma_1$, $\gamma^2 = \sigma_3$ and setting $k_2 = 0$,⁸ after which one finds two sets of decoupled equations

$$\sqrt{\frac{g_{ii}}{g_{rr}}} (\partial_r \mp m \sqrt{g_{rr}}) y_\pm = \mp i (k_1 - u) z_\mp, \quad (20)$$

$$\sqrt{\frac{g_{ii}}{g_{rr}}} (\partial_r \pm m \sqrt{g_{rr}}) z_\mp = \pm i (k_1 + u) y_\pm \quad (21)$$

where we have written

$$\phi_\pm = \begin{pmatrix} y_\pm \\ z_\pm \end{pmatrix}.$$

Introducing the ratios

$$\xi_+ = \frac{i y_-}{z_+}, \quad \xi_- = -\frac{i z_-}{y_+}, \quad (22)$$

and using (19), the retarded Green function G_R can be written as

$$G_R = \lim_{\epsilon \rightarrow 0} \epsilon^{-2m} \begin{pmatrix} \xi_+ & 0 \\ 0 & \xi_- \end{pmatrix} \Big|_{r=(1/\epsilon)}, \quad (23)$$

where one should extract the finite terms in the limit.

It is convenient to derive flow equations directly for ξ_\pm as in [16]. From (20), we find

$$\sqrt{\frac{g_{ii}}{g_{rr}}} \partial_r \xi_\pm = -2m \sqrt{g_{ii}} \xi_\pm \mp (k_1 \mp u) \pm (k_1 \pm u) \xi_\pm^2. \quad (24)$$

The in-falling boundary condition at the horizon implies

$$\xi_\pm|_{r=1} = i. \quad (25)$$

With the boundary condition (25), one can now integrate (24) to $r \rightarrow \infty$ to obtain the boundary correlation function directly. Below we will drop the subscript 1 on k_1 .

At zero temperature, the $\omega \rightarrow 0$ limit of Eqs. (20), (21), and (24) is singular, since g_{tt} then has a double zero at the horizon. As we will see this has important consequences for the behavior of G_R near $\omega = 0$. Also, at $\omega = 0$ the in-falling boundary conditions (25) do not apply and should be replaced by

$$\xi_\pm|_{r=1, \omega=0} = \frac{-m - \sqrt{k^2 + m^2 - \frac{\mu_q^2}{6} - i\epsilon}}{\frac{\mu_q}{\sqrt{6}} \mp k}. \quad (26)$$

Note that the $1/\sqrt{6}$ factor multiplying μ_q in (26) has the same origin as the one appearing in (9).

⁸Since the system is rotationally symmetric, there is no loss of generality.

III. PROPERTIES OF SPECTRAL FUNCTIONS

A. General behavior

We now describe the properties of G_R obtained by solving (24). First note that by taking $k \rightarrow -k$ the equations for ξ_{\pm} exchange with each other, leading to

$$G_{22}(\omega, k) = G_{11}(\omega, -k). \quad (27)$$

Similarly by taking $q \rightarrow -q$, $\omega \rightarrow -\omega$ we find that

$$G_{11}(\omega, k; -q) = -G_{22}^*(-\omega, k; q). \quad (28)$$

So it is enough to restrict to positive k and q . One can also check that as $|\omega|, |k| \gg \mu_q$, both components reduce to those of the vacuum. When $m = 0$, by dividing the equation for ξ_+ in (24) by ξ_+^2 , we find that $\xi_- = -\frac{1}{\xi_+}$, which implies that

$$G_{22}(\omega, k) = -\frac{1}{G_{11}(\omega, k)}, \quad m = 0. \quad (29)$$

Combining (27) and (29) we thus conclude that at $k = 0$,

$$G_{11}(\omega, k = 0) = G_{22}(\omega, k = 0) = i, \quad m = 0. \quad (30)$$

Further study of G_R is possible by numerically solving (24). We will first consider $T = 0$ and will mostly discuss the mass dependence. The mass dependence will be discussed

briefly at the end. There are several consistency checks on our numerics. First, $\text{Im}G_{11}$ and $\text{Im}G_{22}$ are both positive, which is a requirement of unitarity since the diagonal components are proportional to spectral densities. For a fixed large $k \gg \mu_q$, $\text{Im}G_{11}$ has a linearly-dispersing constant-height peak at $\omega + \mu_q \approx -k$ and $\text{Im}G_{22}$ has a peak at $\omega + \mu_q \approx k$, while both components are roughly zero in the region $\omega + \mu_q \in (-k, k)$ (see Figs. 1 and 2). This recovers the behavior in the vacuum, which is given by [21,22]

$$G_{11} = -\sqrt{\frac{k - (\omega + i\epsilon)}{k + (\omega + i\epsilon)}}, \quad G_{22} = \sqrt{\frac{k + (\omega + i\epsilon)}{k - (\omega + i\epsilon)}} \quad (31)$$

with now the divergences at $\omega = \pm k$ smoothed out into finite size peaks.

B. Fermi surface

As one decreases k to μ_q and smaller, the behavior of G_R deviates significantly from that of the vacuum. For definiteness, let us now focus on $q = 1$ (with $\mu_q = \sqrt{3}$). In this case the finite peak of $\text{Im}G_{22}$ in the large k region develops into a sharp quasi-particle-like peak near $k_F = 0.918528499(1)$ (see Fig. 2). The behavior of $\text{Im}G_{22}$

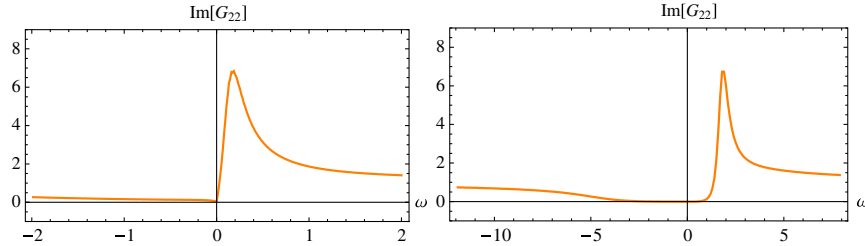


FIG. 1 (color online). Spectral function $\text{Im}G_{22}(\omega)$ at $k = 1.2 < \mu_q$ (left plot) and $k = 3.0 > \mu_q$ (right plot) for $m = 0$ and $q = 1$ ($\mu_q = \sqrt{3}$). The function asymptotes to 1 as $|\omega| \rightarrow \infty$ as in the vacuum (31). Right plot: The onset of the finite peak at $\omega \approx 1.2 \approx k - \mu_q$ roughly corresponds to the location of divergence at $\omega = k$ in the vacuum (31). The function is roughly zero between $\omega \in (-k - \mu_q, k - \mu_q)$, as it is in vacuum. Left plot: The deviation from the vacuum behavior becomes significant.

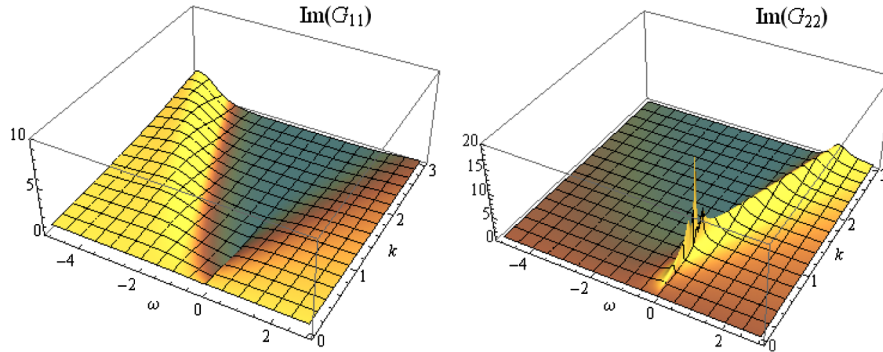


FIG. 2 (color online). 3d plots of $\text{Im}G_{11}(\omega, k)$ and $\text{Im}G_{22}(\omega, k)$ for $m = 0$ and $q = 1$ ($\mu_q = \sqrt{3}$). In the right plot the ridge at $k \gg \mu_q$ corresponds to the smoothed-out peaks at finite density of the divergence at $\omega = k$ in the vacuum. As one decreases k to a value $k_F \approx 0.92 < \mu_q$, the ridge in $\text{Im}G_{22}$ develops into an (infinitely) sharp peak indicative of a Fermi surface.

in the region of small $k_{\perp} \equiv k - k_F$ and ω can be summarized as follows:

- (1) For $k_{\perp} < 0$, we find a sharp quasi-particle-like peak in the region $\omega < 0$ and a small ‘‘bump’’ (with a broad maximum) in the region $\omega > 0$ (see Fig. 3). This appears to indicate that there is a quasi-particle-like pole in the left quadrant of the lower-half complex ω -plane. As $k_{\perp} \rightarrow 0_-$, both the peak and the maximum of the bump approach $\omega = 0$, their heights go to infinity, and their widths go to zero. By carefully examining when the peak and the bump meet we are able to determine the accuracy of $k_F = 0.918528499(1)$ to 10th digit.
- (2) For $k_{\perp} > 0$, one does *not* see a sharp peak along real ω -axis for either sign of ω . Instead one finds a bump (with a broad maximum) on the $\omega > 0$ side and a smaller bump on the $\omega < 0$ side. See Fig. 4. In the limit $k_{\perp} \rightarrow 0_+$, both bumps approach $\omega = 0$ and their heights go into infinity.
- (3) The quasi-particle-like peak and various bumps can also be studied by plotting $\text{Im}G_{22}(k, \omega)$ as a function of k for a given ω (see the left panel of Fig. 5 for a plot at $\omega = -0.001$). In the limit $\omega \rightarrow 0_-$, the height of the peak goes to infinity with its width going to zero. At exactly $\omega = 0$, however, the functions $\text{Im}G_{11}$ and $\text{Im}G_{22}$ become identically zero for $k > \frac{\mu_q}{\sqrt{6}} = \frac{1}{\sqrt{2}}$ (see the right panel of Fig. 5). This behavior can be understood from (26) and (24) as follows. For $k \geq \frac{\mu_q}{\sqrt{6}}$ (at $m = 0$), the boundary conditions (26) become real and since (24) are real equations, $\text{Im}G_{ii}(\omega = 0, k)$ are then identically zero in this region. Note that $k_F > \frac{1}{\sqrt{2}}$.

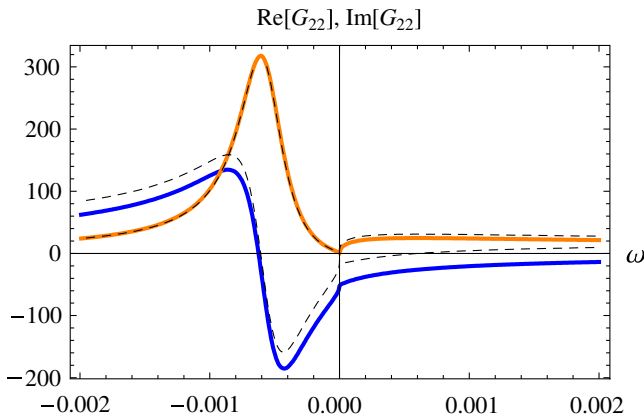


FIG. 3 (color online). $\text{Re}G_{22}(\omega)$ (blue) and $\text{Im}G_{22}(\omega)$ (orange, positive curve) at $k = 0.90 < k_F$. In $\text{Im}G_{22}$, at $\omega < 0$ there is a quasi-particle-like peak; for $\omega > 0$, there is a much smaller ‘‘bump.’’ As k approaches k_F , the peak and the bump approach $\omega = 0$ and their heights approach infinity. The dashed lines are the real and imaginary parts of the fit function (36). Although the real part slightly deviates from the fit, there is a qualitative match.

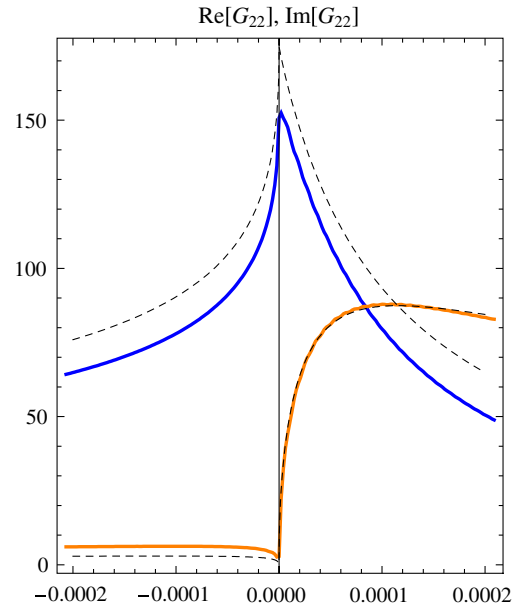


FIG. 4 (color online). $\text{Re}G_{22}(\omega)$ (blue curve with peak near origin) and $\text{Im}G_{22}(\omega)$ (orange) at $k = 0.925 > k_F$. One finds a bump at $\omega > 0$ and a much smaller bump at $\omega < 0$. As k_{\perp} approaches 0_+ , both bumps approach $\omega = 0$ and their heights approach infinity. The dashed lines are the real and imaginary parts of the fit function (39). The fit is not so good for $\omega < 0$, though the qualitative trend matches.

Denoting the location of the maximum of the quasi-particle-like peak as $\omega_*(k_{\perp})$ we find that $\omega_*(k_{\perp})$ scales with $k_{\perp} \rightarrow 0_-$ as

$$\omega_*(k_{\perp}) \sim k_{\perp}^z, \quad z = 2.09 \pm 0.01 \quad (32)$$

and the height of $\text{Im}G_{22}$ at the maximum scales as

$$\text{Im}G_{22}(\omega_*(k_{\perp}), k_{\perp}) \sim k_{\perp}^{-\alpha}, \quad \alpha = 1.00 \pm 0.01 \quad (33)$$

(see Fig. 6). One finds exactly the same scaling behavior also for the maxima of the other three ‘‘bumps.’’ This strongly suggests that in the limit of small k_{\perp} and ω $\text{Im}G_{22}(\omega, k_{\perp})$ has the following scaling form

$$\text{Im}G_{22}(\lambda^z \omega, \lambda k_{\perp}) = \lambda^{-\alpha} \text{Im}G_{22}(\omega, k_{\perp}) \quad (34)$$

with the scaling exponents α, z given by

$$z = 2.09 \pm 0.01, \quad \alpha = 1.00 \pm 0.01. \quad (35)$$

The scaling behavior (32)–(35) suggests an underlying sharp Fermi surface with Fermi momentum k_F . It is, however, not of the form corresponding to a *Landau* Fermi liquid which would have exponents $z = \alpha = 1$. It is an example of the more general scaling behavior discussed recently by Senthil [23,24] for a critical Fermi surface occurring at a continuous metal-insulator transition.⁹ The system also has a rather curious particle-hole asymmetry; the quasi-particle-like peak at $k_{\perp} < 0$ morphs into a bump at $k_{\perp} > 0$ as the Fermi surface is crossed (compare feature

⁹For early work, see [25,26].

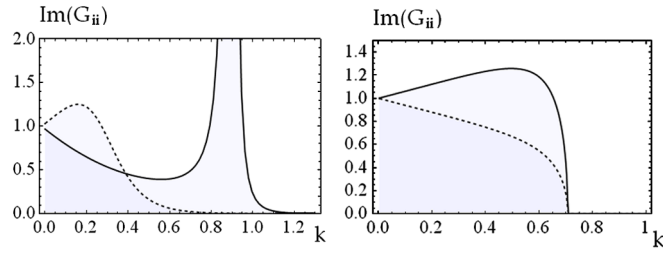


FIG. 5 (color online). Left: Plots of $\text{Im}G_{11}(k)$ (dashed line) and $\text{Im}G_{22}(k)$ as a function of k at $\omega = -0.001$ ($m = 0$ and $q = 1$). A sharp peak in $\text{Im}G_{22}(k)$ is clearly visible near $k_F \approx 0.9185$. The height of the peak is finite. In the limit $\omega \rightarrow 0_-$, the height of the peak goes to infinity and the location of the peak approaches k_F from left. Right: Plots of $\text{Im}G_{11}(k)$ (dashed line) and $\text{Im}G_{22}(k)$ as a function of k at $\omega = 0$. For $\omega = 0$, both functions become identically zero in the region $k > \frac{\mu_q}{\sqrt{6}} = \frac{1}{\sqrt{2}}$. Since $k_F > 1/\sqrt{2}$, at $\omega = 0$, $\text{Im}G_{22}$ is identically zero around k_F .

1 and 2 of previous page). The fact that $\mu_q > k_F$ suggests that the system has repulsive interactions.

For a given $\omega \neq 0$, $G_{ii}(k, \omega)$ are nonsingular for any value of k including k_F , while for a given value of k , $G_{ii}(k, \omega)$ is continuous but nonsmooth at $\omega = 0$.¹⁰ This nonsmooth behavior at $\omega = 0$ for momenta away from the Fermi momentum is puzzling and it would be nice to understand its physical interpretation better. From the gravity side, this is related to the aforementioned singular behavior of Eqs. (20), (21), and (24) near $\omega \rightarrow 0$, as discussed around (26). This can be further attributed to the existence of an AdS_2 region (9) in the bulk geometry at zero temperature.

Further support for the scaling behavior (34) near the Fermi surface can be obtained by fitting the whole curves of $G_{22}(\omega)$ (rather than just the behavior near the maxima) for different k_\perp by a scaling function which is analytic in the upper half ω -plane^{11,12}:

- (1) For $k_\perp < 0$, G_{22} can be fitted¹³ for both signs of ω , by (see Fig. 3)

$$G_{22}(\omega, k_\perp) \approx \frac{c_0(-k_\perp)^{-\alpha}}{\log\left(\frac{-\omega}{c_1(-k_\perp)^2}\right) - i\gamma} \quad (36)$$

where $\gamma \approx 0.34$ and c_0, c_1 are positive constants (in the scaling region). The above function has a pole in the lower-half ω -plane at

¹⁰From numerical calculation, it does appear that the functions become smoother for $k \gg \mu_q$.

¹¹We would like to thank S. Sachdev for a discussion of possible subtleties.

¹²The following discussion of numerical fits is superseded by the analysis of [27] where the exact functional form near the Fermi surface is found.

¹³The function fits well not only along the real ω -axis, but also in the upper half plane. There are numerical instabilities at zero temperature in the lower half complex ω -plane and we have not been able to perform a direct fit there.

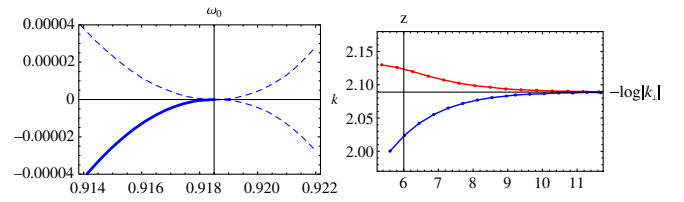


FIG. 6 (color online). Left plot: Dispersion relation $\omega_*(k) \sim k_\perp^z$ around k_F . The dashed lines indicate the ω -values of the maxima of the bumps. The solid line shows the dispersion of the quasiparticle peak. Right plot: Convergence of the z scaling exponent for $k > k_F$ (red, upper curve) and $k < k_F$ (blue). The horizontal axis is the natural log of k_\perp .

$$\omega_c = -c_1(-k_\perp)^z e^{i\gamma}. \quad (37)$$

As $k_\perp \rightarrow 0_-$, ω_c approaches to the origin of the complex plane along a straight line which has an angle $\gamma - \pi$ with respect to the positive real axis. Since $\text{Re}\omega_c$ gives the location $\omega_*(k_\perp)$ of the peak and $-\text{Im}\omega_c$ gives the width Γ of the peak, for (36),

$$\Gamma = \tan\gamma|\omega_*(k_\perp)|. \quad (38)$$

This linear dependence of the width on ω_* ¹⁴ is reminiscent of the behavior in e.g. [2].

- (2) For $k_\perp > 0$, we have not found a good global fit for both signs of ω . A reasonable fit for the imaginary part is

$$G_{22}(\omega, k_\perp) \approx \frac{a_0 k_\perp^{-\alpha}}{a_1 - i\left(\frac{|\omega|}{k_\perp}\right)^{\alpha/z}}; \quad (39)$$

where a_0 and a_1 are positive constants which take different values for $\omega < 0$ and $\omega > 0$.¹⁵ It is important to note that the functions (36) and (39) are only best numerical fits we could find and should not be taken too seriously as the “genuine” functions which describe the system. Both are consistent with the requirement from Fig. 5 that $\text{Im}G_{22}(k_\perp) = 0$ at $\omega = 0$. The different fit functions for $k_\perp < 0$ and $k_\perp > 0$ may reflect the “particle-hole asymmetry” discussed earlier. Also note that for a nonzero k_\perp both (36) and (39) indicate a branch point singularity at $\omega = 0$, but have different $k_\perp \rightarrow 0$ limits. The behavior of $\text{Im}G_{22}(\omega)$ at exactly $k = k_F$ is not completely clear to us at the moment.

C. Discrete scale invariance

In the region $k < \frac{\mu_q}{\sqrt{6}}$, where $\text{Im}G_{ii}(\omega = 0, k)$ are non-zero (see Fig. 5), a new phenomenon occurs in the $\omega \rightarrow 0$ limit. One finds that $\text{Im}G_{ii}(\omega, k)$ become oscillatory with

¹⁴Recall that for a Landau quasiparticle, $\Gamma \sim \omega_*^2$.

¹⁵Again we are handicapped by a numerical instability in the lower half ω -plane which prevents a fit directly around the singularities in the lower half plane.

oscillatory peaks periodic in $\log|\omega|$ with constant heights, see Fig. 7. More explicitly we find

$$G_{ii}(\omega, k) = G_{ii}(\omega e^{n\xi(k)}, k), \quad n \in \mathbb{Z}, \quad \omega \rightarrow 0 \quad (40)$$

where $\xi(k)$ is a (k -dependent) positive constant. In other words, G_{ii} is invariant under a discrete scaling in ω . $\xi(k)$ appears to decrease with k and approaches a constant in the limit $k \rightarrow 0$. In the limit $k \rightarrow \frac{\mu_q}{\sqrt{6}}$, $\xi(k)$ approaches infinity. The height of the oscillatory peaks also decreases with k , approaching zero as $k \rightarrow 0$ (where the whole function approaches unity) and a finite constant as $k \rightarrow \frac{\mu_q}{\sqrt{6}}$. It would be interesting to understand whether (40) is associated with some kind of complex scaling exponents. Below we will refer to the region $k < \frac{\mu_q}{\sqrt{6}}$ as the oscillatory region. Note that the oscillatory region appears to be the counterpart for fermions of the unstable region for a charged boson, where the corresponding bosonic modes have complex energies and want to condense. In the fermion case, the oscillatory region does not appear to indicate an instability, e.g. there is no singularity in the upper half of the complex ω -plane.

D. Finite temperature

Turning on a small temperature T appears to smooth everything out. There is no longer a sharp Fermi surface, i.e. there no longer exists a sharp momentum at which $\text{Im}G_{22}$ becomes singular for any real ω and k . Going to the lower half ω -plane, one finds that all the singularities are a finite distance away from the real axis, with the closest distance given by T which happens at $k \approx 0.90$ (see Fig. 8).¹⁶ This behavior is different from the Fermi liquid where the width is quadratic in temperature. Note that for a given small $k_{\perp} < 0$, as one turns on the temperature, the corresponding quasi-particle-like pole in the complex ω -plane appears to move down and to the right. It is also interesting to note that at finite T , there are now quasi-particle-like poles for momenta $k > k_F$. Perhaps they are generated from the branch point at $T = 0$.

At finite T , the functions $\text{Im}G_{ii}$ become smooth at $\omega = 0$ and in the oscillatory region there are only a finite number of oscillations as the $\omega \rightarrow 0$ limit is approached.

E. Charge dependence

When we increase (decrease) q to be greater (smaller) than 1, the Fermi momentum k_F increases (decreases) with q approximately linearly. As q is further increased, new branches of Fermi surfaces appear. These features can be seen in Fig. 9, which gives the density plots of $\text{Im}G_{11}$ and $\text{Im}G_{22}$ in the $q - k$ plane at a fixed value of $\omega = -0.001$.

We have sampled the exponents z, α for a few other values of q for the lowest branch of Fermi surface in

¹⁶Similar results have also been obtained by Carlos Fuertes. We thank Carlos Fuertes and Subir Sachdev for communicating the results to us.

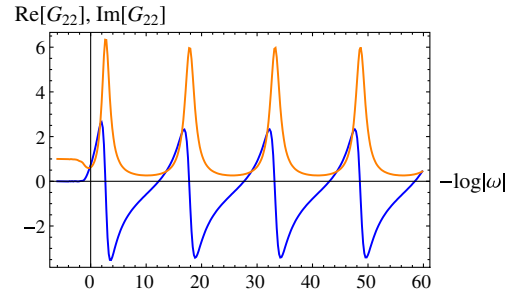


FIG. 7 (color online). Both $\text{Re}G_{22}(\omega, k = 0.5)$ (blue curve) and $\text{Im}G_{22}(\omega, k = 0.5)$ (orange, positive curve) are periodic in $\log\omega$ as $\omega \rightarrow 0$. The period appears to be given by $\Delta(\log\omega) \approx \frac{\pi\sqrt{6}}{\sqrt{\mu_q^2/6 - (k^2 + m^2)}}$. This formula was guessed based on the behavior of the solution in the AdS_2 region; the formula is confirmed by the numerics.

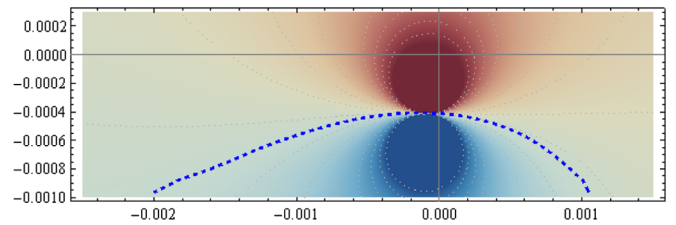


FIG. 8 (color online). The complex omega plane for $T = 4.13 \times 10^{-4}$; now the quasiparticle pole is finite distance below the real ω -axis. The dashed line indicates the trajectory of the pole between $k = 0.87$ (left) ... 0.93 (right). The closest distance to the real axis is equal to the temperature T (up to 1% accuracy). There is a numerical instability for $\text{Im}\omega < -\pi T$ which can also be seen directly from the wave equation. We leave it for future work to explore this part of the lower half plane. Also shown is the density plot for $\text{Im}G_{22}(\omega)$ at $k = 0.90$, where the corresponding pole is closest to the real axis.

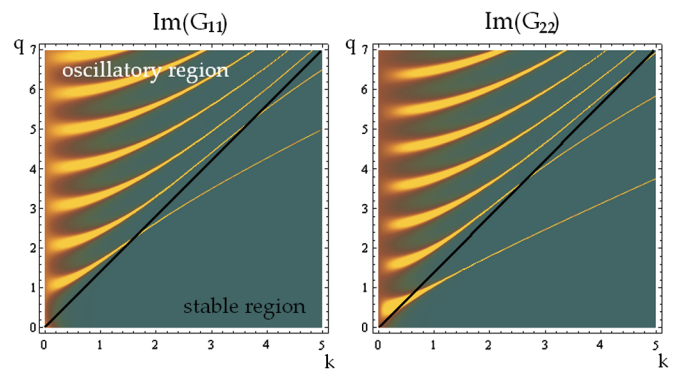


FIG. 9 (color online). Density plot of $\text{Im}G_{ij}(k, q)_{\omega=-0.001}$ with $k \in [0, 5]$ and $q \in [0, 7]$ at $T = 2.76 \times 10^{-6}$. A negligible temperature was turned on in order to increase the speed of the computation. The results were not affected by this. The orange lines are locations where the functions become very large. Also note that the width of the peaks in $\text{Im}G(k)$ decreases quickly as one moves towards larger charge. The black line is $k = \mu_q/\sqrt{6}$ to the left of which is the oscillatory region.

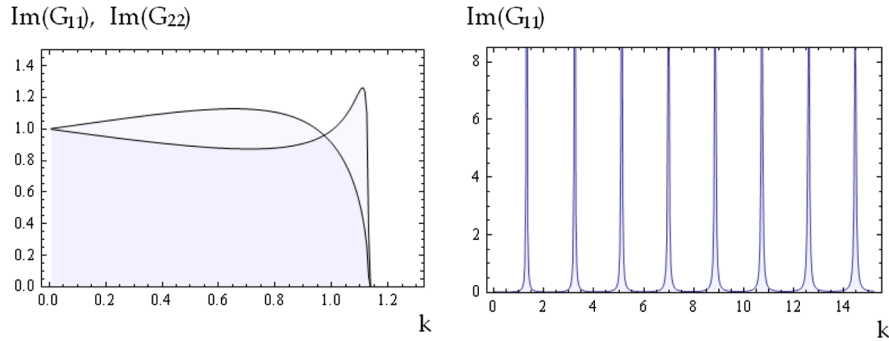


FIG. 10 (color online). (i) $\text{Im}G_{ij}(k)_{\omega=0}$ with $q = 1.6$. Near $k = \mu_q/\sqrt{6}$, a bump is seen in $\text{Im}G_{22}(k)$. At slightly higher value of the charge, the Fermi surface crosses the boundary of the oscillatory region and this bump becomes a peak. (ii) $\text{Im}G_{11}(q, k)_{\omega=0}$ along the $\mu_q = \sqrt{6}k$ line. The spacing between the peaks is constant, $\Delta k \sim \sqrt{7/2}(\pm 1\%)$.

$\text{Im}G_{22}$, e.g. for $q = 0.6$, $z \approx 5.32$, $\alpha \approx 1.00$, and for $q = 1.2$, $z \approx 1.53$, $\alpha \approx 1.00$. Compared to the values for $q = 1$ described earlier, it then appears that z decreases rapidly with increasing q , while $\alpha = 1$ is independent of q . Note that in [23] it was argued that $z \geq \alpha$ and $z \geq 1$. Thus it could be that z will asymptote to 1 for larger values of q .¹⁷ We also find that the constant γ in (36) appears to decrease rapidly with q . Thus it seems likely that as q is increased, the non-Fermi liquid will become more like a Landau Fermi liquid. Given that k_F increases with q , this is reminiscent of asymptotic freedom in high-density QCD.

The $q - k$ space in Fig. 9 is separated into two regions by the (black) $k = \frac{\mu_q}{\sqrt{6}}$ line. In the region to the right (stable region), the locations of the quasiparticle lines (i.e. orange lines in Fig. 9) stabilize in the limit $\omega \rightarrow 0$ and indicate locations of Fermi surfaces. The region to the left is the oscillatory region discussed earlier, where the log-periodic oscillatory behavior is reflected in a downward motion of the orange lines as $|\omega|$ is decreased; they seem to become infinitely dense in the limit $\omega \rightarrow 0$. Also recall that in the oscillatory region, the heights of the peaks remain finite in the $\omega \rightarrow 0$ limit.

As one decreases q , a Fermi surface line in Fig. 9 will intersect the line $k = \frac{\mu_q}{\sqrt{6}}$, disappear into the oscillatory region, and lose its status as a Fermi surface. Thus the behavior of $\text{Im}G_{ii}$ in the oscillatory region is strongly correlated with the sprouting of new branches of Fermi surface as q is varied (see Fig. 10).

We have also studied other values of the mass (with $m < \frac{1}{2}$) at $q = 1$, and find the Fermi momentum k_F decreases linearly with increasing mass. At finite mass, the oscillatory region is now given by $k^2 + m^2 < \frac{\mu_q^2}{6}$ (see (26)). We find that for $q = 1$, the Fermi surface disappears into the oscillatory region at roughly $m \approx 0.4$. For $m > \frac{\mu_q}{\sqrt{6}}$, the

oscillatory region disappears; we expect the Fermi surface will also disappear beyond this value if not before.

F. Summary

To conclude this section, let us summarize the main features of the spectral functions which we have observed. The system we study is conformally invariant at zero density. Turning on a finite charge density breaks Lorentz and scale invariance. The energy scale of the problem is controlled by the chemical potential μ which for a charge q particle becomes $\mu_q = \mu q$. At $q = 1$ the spectral functions also exhibit two other interesting scales. The first is the Fermi momentum $k_F < \mu_q$ around which we observe a quasi-particle-like peak which suggests an underlying Fermi surface. The scaling behavior and the particle-hole asymmetry around the Fermi surface indicate that this is a non-Fermi liquid. The other scale is $k_S \equiv \frac{\mu_q}{\sqrt{6}}$, which lies below k_F . We find that for $k < k_S$, the spectral functions have log-periodic oscillatory behavior near $\omega = 0$, which indicates some underlying discrete scale invariance. At larger values of q new scales corresponding to more branches of Fermi surface also appear.

It is important to emphasize that the scaling behavior observed here is not related to the scale invariance of the vacuum, which is broken by the nonzero charge density. It is emergent, arising as a consequence of the collective behavior of many particles. Note that both the scaling behavior around the Fermi surface and the discrete scale invariance involve the small ω limit, which on the gravity side can be attributed to the AdS_2 region in the near horizon geometry of the black hole at zero temperature. It may be possible that this emergent scaling behavior can be understood from the AdS_2 region.¹⁸

IV. DISCUSSION

Finally, we discuss some caveats and possible interpretation of the results. While the black hole geometry (6) is

¹⁷At larger values of q the convergence of the exponents becomes slower; we leave this for future work. Also note that the value $\alpha = 1$ is special according to the scaling theory of [23].

¹⁸Work in progress with T. Faulkner [27].

by itself thermodynamically and perturbatively stable, when it is embedded into a specific gravity theory, new instabilities may occur. For example, it is possible for charged (bulk) scalars to condense, spontaneously breaking the $U(1)$ symmetry [28,29]. This happens if the bulk spectrum includes a charged scalar of sufficiently large charge or sufficiently small mass [30]. The boundary theories considered in [30] all contain such scalars including the $\mathcal{N} = 8$ M2 brane theory and ABJM theory. It would be very interesting to understand how the condensate affects the Fermi surfaces and scaling behavior observed here, and how generic the existence of such scalars is.

The black hole solution (6) has a finite entropy at zero temperature, and thus describes an ensemble of an exponentially large number of states. Given that the solution is not supersymmetric, it is likely that beyond the classical gravity approximation these states are energetically closely-spaced, rather than exactly degenerate. This “frustrated property” is shared by many known models of spin liquids. The behavior described above then reflects average behavior of a large number of states rather than that of a single ground state.

A rather mysterious feature of our results is that different probe operators appear to find different Fermi surface structure which depends on (and only on) their charges and operator dimensions. One possible explanation is as follows.¹⁹ Let us look at the OPE of *e.g.* the first component \mathcal{O}_1 of a fermionic operator \mathcal{O} , which has the schematic form

$$\mathcal{O}_1(\epsilon)^\dagger \mathcal{O}_1(0) \sim \frac{1}{\epsilon^{2\Delta}} + \frac{c(\Delta)}{N^2} \frac{qJ^0}{\epsilon^{2\Delta-2}} + \dots, \quad (41)$$

where J^0 is the zero component of global $U(1)$ current. Equation (41) implies that the density for \mathcal{O}_1 can be written as

$$n_{\mathcal{O}_1} = \langle \mathcal{O}_1(\epsilon)^\dagger \mathcal{O}_1(0) \rangle \sim \frac{1}{\epsilon^{2\Delta}} + \frac{c(\Delta)}{N^2} \frac{q\langle J^0 \rangle}{\epsilon^{2\Delta-2}} + \dots \quad \epsilon \rightarrow 0 \quad (42)$$

where ϵ should be considered as a short-distance cutoff. The first term on RHS of (42) is the standard piece due to vacuum fluctuations, which can be subtracted. In a state of finite density, the second term induces a density for \mathcal{O}_1 , which is proportional to q , the background charge density and depends on the UV cutoff through the dimension of the operator. Since the Fermi surface involves modes with wavelengths of order k_F^{-1} , which is parametrically distinct from the short wavelength of the modes contributing the UV divergence, we expect that the fermionic density which is responsible for the Fermi surface should be insensitive to

¹⁹We would like to thank T. Senthil for long and very instructive discussions about this.

the UV cutoff. The background charge density $\langle J^0 \rangle \propto N^2$ induces a nonzero charge density of order $O(N^0)$ for each charged operator, which depends on its charge and conformal dimension. The induced density increases with its charge, which is consistent with our empirical observation that k_F increases with the charge of the bulk particle.

In the large N limit, the effective interactions of \mathcal{O} with itself and other gauge invariant operators are all suppressed by $1/N$. This may lead one to conclude that the effective theory for \mathcal{O} should be a free Fermi gas, which would contradict our observed scaling behavior near k_F . Note, however, the effective dynamics of \mathcal{O} can be different from that of a free fermion, again due to large N effects. To see this, let us look at the current density from \mathcal{O} , which can be schematically written as $j^\mu = \bar{\mathcal{O}}\gamma^\mu\mathcal{O}$. The fluctuations of j^μ , which can be read from its connected two point functions, are suppressed by $1/N^2$. Thus in the large N limit, j^μ does not fluctuate. One can try to model this by coupling a free fermion to a gauge field, which acts as a Lagrange multiplier suppressing the fluctuations of the associated current. When coupling a Fermi liquid to a dynamical gauge field, it is well known (see *e.g.* [31–40]) that long-range magnetic interactions result in a non-Fermi liquid, which appears to be consistent with our picture. It would be desirable to make this argument more precise. Note that the particle-hole asymmetry is not seen in previously known models. The above suggestion does not preclude the existence of some fundamental non-Fermi liquid structure from which the behavior of probe fermionic operators could be derived.

The fact that the induced charge density for each probe operator is of order $O(1)$ also implies that their contributions to the transport of the system are not visible at leading order in the large N expansion. Indeed, to leading order in N none of the observables like specific heat, conductivity, entanglement entropy can depend on the charge or dimension of probe spinor fields. However, if there exists a fundamental non-Fermi liquid structure, some effects might still be visible at leading order. We will leave this for future study.

Finally, as indicated earlier, the near horizon AdS_2 region appears to play a role for the appearance of both the log-periodic behavior in the oscillatory region and the Fermi-surfaces. Clearly it would be interesting to have a better understanding of the CFT interpretation of the AdS_2 region.

ACKNOWLEDGMENTS

We thank T. Faulkner, C. Fuertes, S. Hartnoll, N. Iqbal, V. Khodel, P. Lee, M. Mulligan, K. Rajagopal, S. Sachdev, S. Shenker, B. Swingle, G. Volovik, B. Zwiebach and, in particular, T. Senthil for valuable discussions and encouragement. Work supported in part by funds provided by the U.S. Department of Energy (D.O.E.) under cooperative research agreement DE-FG0205ER41360 and the OJI program.

- [1] P.W. Anderson, *Phys. Rev. Lett.* **64**, 1839 (1990).
- [2] C.M. Varma, P.B. Littlewood, S. Schmitt-Rink, E. Abrahams, and A.E. Ruckenstein, *Phys. Rev. Lett.* **63**, 1996 (1989).
- [3] C.M. Varma, Z. Nussinov, and W. van Saarloos, *Phys. Rep.* **361**, 267 (2002).
- [4] G. Benfatto and G. Gallavotti, *J. Stat. Phys.* **59**, 541 (1990).
- [5] R. Shankar, *Physica A (Amsterdam)* **177**, 530 (1991).
- [6] J. Polchinski, arXiv:hep-th/9210046.
- [7] R. Shankar, *Rev. Mod. Phys.* **66**, 129 (1994).
- [8] J.M. Maldacena, *Adv. Theor. Math. Phys.* **2**, 231 (1998).
- [9] S.S. Gubser, I.R. Klebanov, and A.M. Polyakov, *Phys. Lett. B* **428**, 105 (1998).
- [10] E. Witten, *Adv. Theor. Math. Phys.* **2**, 353 (1998).
- [11] J. Bagger and N. Lambert, *J. High Energy Phys.* **02** (2008) 105.
- [12] A. Gustavsson, *Nucl. Phys.* **B811**, 66 (2009).
- [13] O. Aharony, O. Bergman, D.L. Jafferis, and J. Maldacena, *J. High Energy Phys.* **10** (2008) 091.
- [14] S.-S. Lee, *Phys. Rev. D* **79**, 086006 (2009).
- [15] D.T. Son and A.O. Starinets, *J. High Energy Phys.* **09** (2002) 042.
- [16] N. Iqbal and H. Liu, *Phys. Rev. D* **79**, 025023 (2009).
- [17] N. Iqbal and H. Liu, *Fortschr. Phys.* **57**, 367 (2009).
- [18] A. Chamblin, R. Emparan, C.V. Johnson, and R.C. Myers, *Phys. Rev. D* **60**, 064018 (1999).
- [19] L.J. Romans, *Nucl. Phys.* **B383**, 395 (1992).
- [20] J.P. Gauntlett and O. Varela, *Phys. Rev. D* **76**, 126007 (2007).
- [21] M. Henningson and K. Sfetsos, *Phys. Lett. B* **431**, 63 (1998).
- [22] W. Mueck and K.S. Viswanathan, *Phys. Rev. D* **58**, 106006 (1998).
- [23] T. Senthil, *Phys. Rev. B* **78**, 035103 (2008).
- [24] T. Senthil, *Phys. Rev. B* **78**, 045109 (2008).
- [25] L. Yin and S. Chakravarty, *Int. J. Mod. Phys. B* **10**, 805 (1996).
- [26] S. Chakravarty, L. Yin, and E. Abrahams, *Phys. Rev. B* **58**, R559 (1998).
- [27] T. Faulkner, H. Liu, J. McGreevy, and D. Vegh, arXiv:0907.2694.
- [28] S.S. Gubser, *Phys. Rev. D* **78**, 065034 (2008).
- [29] S.A. Hartnoll, C.P. Herzog, and G.T. Horowitz, *Phys. Rev. Lett.* **101**, 031601 (2008).
- [30] F. Denef and S.A. Hartnoll, *Phys. Rev. D* **79**, 126008 (2009).
- [31] T. Holstein, R.E. Norton, and P. Pincus, *Phys. Rev. B* **8**, 2649 (1973).
- [32] M.Y. Reizer, *Phys. Rev. B* **40**, 11571 (1989).
- [33] J. Polchinski, *Nucl. Phys.* **B422**, 617 (1994).
- [34] B.I. Halperin, P.A. Lee, and N. Read, *Phys. Rev. B* **47**, 7312 (1993).
- [35] C. Nayak and F. Wilczek, *Nucl. Phys.* **B417**, 359 (1994).
- [36] C. Nayak and F. Wilczek, *Nucl. Phys.* **B430**, 534 (1994).
- [37] B.L. Altshuler, L.B. Ioffe, and A.J. Millis, *Phys. Rev. B* **50**, 14048 (1994).
- [38] D. Boyanovsky and H.J. de Vega, *Phys. Rev. D* **63**, 034016 (2001).
- [39] A. Ipp, A. Gerhold, and A. Rebhan, *Phys. Rev. D* **69**, 011901 (2004).
- [40] T. Schafer and K. Schwenzer, *Phys. Rev. D* **70**, 054007 (2004).